JOURNAL OF THERMOPHYSICS AND HEAT TRANSFER
Vol. 35, No. 2, April–June 2021

Parametric Shape Optimization of Pin-Fin Arrays Using a Surrogate Model-Based Bayesian Method

Shinjan Ghosh*
University of Central Florida, Orlando, Florida 32816
Sudeepta Mondal†
Pennsylvania State University, University Park, Pennsylvania 16802
Erik Fernandez‡ and Jayanta S. Kapat§
University of Central Florida, Orlando, Florida 32816
and
Asok Roy¶
Pennsylvania State University, University Park, Pennsylvania 16802

https://doi.org/10.2514/1.T6094

Pin-fin arrays are generally present in trailing-edge regions of gas-turbine blades for internal cooling purposes. An elevated temperature is important to enhance the thermodynamic efficiency of gas-turbine cycles, and internal blade-cooling mechanisms are employed to mitigate material failure at these high temperatures. It is also important to have high heat transfer at a limited pressure drop to ensure that the overall cycle efficiency is not affected by power loss from driving the flow through internal cooling circuits. A pin-fin shape optimization has been carried out, with the array performance efficiency factor as the objective function, using surrogate modeling-based Bayesian methods. Surrogate modeling/machine learning approaches are instrumental in exploring global solutions to optimization problems using an exploration versus exploitation approach. This ensures prudent use of computational resources for computationally expensive computational fluid dynamics simulations. By varying geometric parameters of the pin fins, a three-dimensional design space has been explored to obtain an optimum pin-fin shape that has the maximum efficiency in the developing region of the flow. An improvement in the efficiency parameter of 1.4 times that of the baseline was obtained in a three-row pin-fin case, and the results were compared with those of genetic-algorithm-based optimization (nondominated sorted genetic algorithm–II). Computation time for optimization was saved by 52%, as an optimum was obtained at lower number of iterations when compared to the genetic algorithm approach, with a 1.2% higher objective function value. This shows an improvement in performance of the current novel approach compared to another stochastic method.

Nomenclature

A	=	inlet cross-section area
a, b, c	=	pin geometric parameters
D	=	side length of square baseline
D_h	=	hydraulic diameter of pinned channel
D_{ho}	=	hydraulic diameter of smooth channel
f	=	friction factor
H	=	inlet cross-section height of pinned channel
H_o	=	inlet cross-section height of smooth channel
h	=	convective heat transfer coefficient
k	=	thermal conductivity of air
m	=	mass flow rate
Nu	=	Nusselt number
U	=	average velocity in duct
δp	=	pressure drop
η	=	thermal performance efficiency of pin-fin array
η'	=	normalized thermal performance efficiency
ρ	=	density
w_o	=	inlet cross-section width of smooth channel
w	=	inlet cross-section width of pinned channel

Presented as Paper 2019-3830 at the AIAA Propulsion and Energy 2019 Forum, Indianapolis, IN, August 19–22, 2019; received 19 May 2020; revision received 24 July 2020; accepted for publication 5 September 2020; published online 27 October 2020.

*Graduate Research Assistant, Center for Advanced Turbomachinery and Energy Research; shinjanJU.ucf.edu@knights.ucf.edu. Student Member AIAA.
†Graduate Research Assistant, Department of Mechanical Engineering and Department of Mathematics.
‡Research Assistant Professor, Siemens Energy Center, Center for Advanced Turbomachinery and Energy Research.
§Pegasus Professor and Trustee Chair and Director, Center for Advanced Turbomachinery and Energy Research, Department of Mechanical and Aerospace Engineering. Associate Fellow AIAA.
¶University Distinguished Professor, Department of Mechanical Engineering and Department of Mathematics.

I. Introduction

GAS-TURBINE cycle efficiency can be improved by increasing the hot gas path component temperature. The temperature, however, is limited by component life as well as economic and technological constraints. To prevent thermal failure, gas-turbine blades have inbuilt internal and external means of convective cooling mechanisms. Pins and rib turbulated internal cooling channels are among the common designs used to enhance convective heat transfer by means of high turbulent mixing. The chief objective behind optimum design of such channels is to maintain high heat transfer with minimum coolant use and pressure drop [1]. Bunker [2] summarizes that for aviation engines, 20–30% of compressor air is diverted to the high-pressure turbine for internal cooling purposes. It is important to minimize the power loss due to these cooling circuits since it may nullify the efficiency gained by the increase in blade temperature. Heat transfer augmentation increases with increased turbulence due to the presence of ribs, pin fins, or dimple/protrusions in the internal channels. This increased turbulence level is also responsible for a higher amount of pressure drop. Design optimization plays an important role to obtain configurations of internal cooling channels, which balance between the heat transfer and pressure-drop factors. Webb and Eckert [3] developed an efficiency parameter based on the average Nusselt number and friction factor of high-aspect-ratio geometries with constant mass flow rates. The ratio of the Nusselt number and friction factor represents a compromise between heat transfer in the channel

and power expenditure due to flow of coolant air causing pressure drop across the channel. This efficiency factor has been used in the current study for design optimization.

Pin-fin arrays are commonly used in turbine blade-cooling internal trailing-edge geometries to enhance heat transfer [1,2]. Because of the cramped space in the trailing-edge region, short pin-fin arrays are obtained in the high aspect ratio of such channels. Hence, the pin fins are more functional as turbulators rather than structures that increase surface area for heat exchange. Acceleration of flow in the blockages provided by the pin fins increases heat transfer along with secondary vortex interactions due to trailing-edge separations in such pin fins. In the last three decades, numerous experimental studies have been carried out by varying shapes/sizes and spacing of pin-fin arrays. Chyu [4] studied the heat transfer performance of staggered arrays as opposed to inline arrays, and it was observed that higher heat transfer occurred in staggered arrays, along with a higher-pressure drop as compared to inline arrays. A pin endwall fillet was also found to be undesirable in this study. VanFossen [5] performed heat transfer experiments on two different geometries and obtained an array averaged Nusselt number vs Reynolds number correlation.

Chyu et al. [6] studied the effect of cross-sectional geometric variations of square-, circular-, and diamond-shaped pins on heat transfer and pressure drop. The diamond pins were found to have highest heat transfer, followed by the square and the round pin fins. Due to higher-pressure drop in the sharp-edged geometries, the highest efficiency was obtained in the circular pin fins as a tradeoff between pressure loss and heat transfer enhancement. Streamwise heat transfer was studied by Metzger et al. [7] in staggered arrays. The heat transfer coefficients were found to peak at the third row of pins. Metzger and Haley [8] studied the turbulence characteristics of similar geometries using flow visualizations, which were also consistent with the heat transfer characteristics. Ames and Dvorak [9] performed hot-wire experiments and computational fluid dynamics (CFD) simulations to better understand turbulence-related transport phenomena in staggered pin-fin arrays. Armstrong and Winstanley [10] concluded that pin-fin arrays reach their peak heat transfer coefficients at rows 3–5 and are dependent on the Reynolds number raised to a power of 0.6 to 0.7.

Several studies exist on optimization of fins and other components to improve their thermal performance. Elitism-based [11] and genetic-algorithm-based studies were performed on fin geometries [12–15]. The elitism-based JAYA algorithm was used by Venkata Rao et al. [11] for a multiobjective optimization study of heat pipes. Structural parameters were varied to increase heat transfer and reduce thermal resistance in this work. Multiobjective shape optimization in micro pin-fin arrays were carried out by Reddy et al. [16]. Entropy generation minimization techniques were used by Hamadneh et al. [17] to achieve minimum pressure drop and maximum enhancement of convective heat transfer.

Gradient-based methods have also been used extensively for various thermal-fluid optimization problems. Bezier parameter-based parametric polynomials were used by Eyi et al. [18,19] to optimize hypersonic vehicle designs. Of late, a lot of interest has been shown in the interdisciplinary fields of machine learning assisted modeling and optimization [20–22]. Particularly, surrogate assisted optimization [23,24] has been widely used by different researchers for learning metamodels for computationally expensive experiments/simulations in engineering design. Such design problems often involve optimization of an output objective for which the functional relationships with the inputs are not well defined, and hence they invoke the need of gradient-free optimizers in a black-box setting. These are often referred to as high-dimensional expensive black-box problems [25] for which surrogate statistical models can be learned that, in turn, can serve as reliable estimates for the true functions. Of the different surrogate models used by the researchers, one popular method of modeling nonlinear input output relationships is via a Bayesian nonparametric statistical tool called Gaussian processes (GPs) [26]. A GP is a stochastic process that assumes that any (finite) linear combination of random variables has a multivariate jointly Gaussian probability distribution. GPs can be used to model a wide range of relations between the input parameters and system response without assuming any functional relationship beforehand. Being a Bayesian method, GPs also quantify the uncertainties in predictions resulting from possible measurement/modeling noise and variance associated with estimation of the parameters/hyperparameters in the statistical model. Traditionally, machine learning techniques like neural networks have been widely used as a popular choice in prediction problems by modeling nonparametric input output relationships [27,28]. Despite the simplicity of usage, such techniques generally rely on a huge volume of data, and naive applications of such methods in limited datasets can often result in poor predictive models that lack generalizability due to overfitting. On the other hand, probabilistic ML techniques like Gaussian processes offer the advantages of interpretability and applicability in limited data regimes, and their applications in surrogate-based modeling and optimization have been relatively less explored, particularly in multiphysics problems as discussed in this paper.

II. Mathematical Background and Applications

A. Problem Definition

Chyu et al. [6] experimented with various shapes of pin fins in an array to study the effects on heat transfer and pressure drop. Among the square-, circular-, and diamond-shaped pins, a variation of performance efficiency was obtained. The sharp-edged square and diamond pins had a high heat transfer, but pressure drop was lower in the circular pin fins. For the Reynolds number of 12,000, the square pin was found to have the highest efficiency. The current study uses a baseline case consisting of the same exact square-shaped pins (Fig. 1) and the given flow rate. Spanwise and streamwise distances were both equal to 2.5 times the side of the baseline geometry shape. Each segment of line in the baseline square shape consisted of a three-point circular arc. Hence, changing the coordinates of the midpoints of the trailing edge, leading edge, and sidewall of the square-shaped pin fins gave rise to a variety of shapes as seen in Fig. 2. By varying geometric parameters a, b, and c from 3.2 to 6 mm, a three-dimensional design space has been explored to obtain an optimum pin-fin shape that has the maximum efficiency in the developing region of the flow. Flow simulation of each turbulent heat transfer case requires significant computation time. Usage of a surrogate model-based Bayesian optimization technique ensures intelligent sampling, thereby using the available computation power efficiently.

The aim of the current study was to find the optimum shape of the pins to maximize the thermal performance efficiency parameter [3] [Eq. (1)]

$$\eta = (Nu/Nu_o)/(f/f_o)^{1/3} \tag{1}$$

where $Nu = hD/k$ is the array averaged Nusselt number of the pin-fin array. Traditionally, and in the current study, Nu_o is the average wall surface Nusselt number of a smooth pipe of the same dimensions. Also, $f = (\delta P)/(0.5\rho U^2)$ for the array, and f_o is the friction factor of the smooth duct.

Study of the aforementioned efficiency expression can be found in detail in the work of Webb and Eckert [3]. The power required to pump fluid through an internal channel can be expressed as

$$\text{Power} = (m/\rho)\Delta P = AU(f0.5\rho U^2 L/D_h) \propto fAU^3 \tag{2}$$

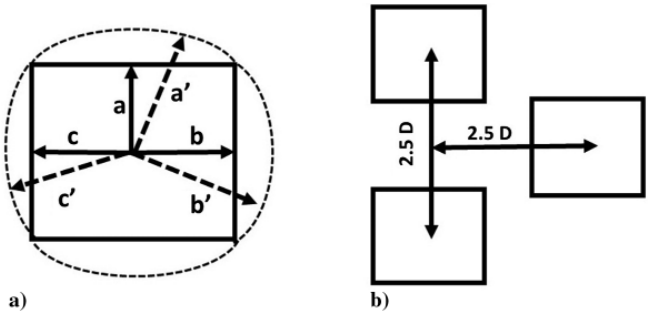

Fig. 1 Representations of a) baseline geometry and parameters definition (for baseline, $a = b = c = 3.2$ mm; a', b', and c' are morphed parameters; and side length $D = 2$ a) and b) layout for pin-fin array (flow from right to left).

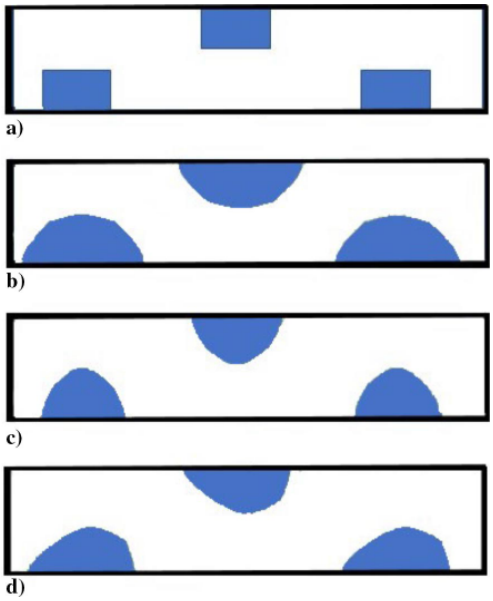

Fig. 2 Different geometries of the pin (flow direction from right to left).

where A is the area of cross section of the channel, and L is the channel length:

$$f_o A_o U_o^3 = fAU^3 \tag{3}$$

For high-aspect-ratio channels with the same area of cross section,

$$f_o/f = AU^3/A_o U_o^3 \tag{4}$$

For high-aspect-ratio channels, $D_h = 2H$, where "H" is the channel height:

$$h/h_o = NukD_h/Nu_o kD_{ho} \simeq (Nu/Nu_o)/(2H_o/2H) \tag{5}$$

Since channel width is constant in current scenario ($w = w_o$), the above equation can be reduced to:

$$\begin{aligned}(Nu/Nu_o)(wU/w_o U_o) &= (Nu/Nu_o)/(U/U_o)\\ &= (Nu/Nu_o)/(f/f_o)^{1/3}\end{aligned} \tag{6}$$

B. Mathematical Background

In this section, a brief overview of the mathematical foundations involved in this paper has been discussed. The surrogate modeling structure in this paper is based on a nonparametric regression technique called Gaussian processes [26]. Gaussian processes assume any finite combination of random variables have a jointly Gaussian distribution. For example, for the function $f(\boldsymbol{x})$ with input $\boldsymbol{x}$, a finite subcollection $\{\boldsymbol{x}_1, \boldsymbol{x}_2, \ldots, \boldsymbol{x}_T\}$ yields the outputs $\{f(\boldsymbol{x}_1), f(\boldsymbol{x}_2), \ldots, f(\boldsymbol{x}_T)\}$ that, by GP assumption, are distributed as jointly Gaussian:

$$\begin{bmatrix} f(\boldsymbol{x}_1) \\ \vdots \\ f(\boldsymbol{x}_T) \end{bmatrix} \sim \mathcal{N}\left(\begin{bmatrix} m(\boldsymbol{x}_1) \\ \vdots \\ m(\boldsymbol{x}_T) \end{bmatrix}, \begin{bmatrix} k(\boldsymbol{x}_1, \boldsymbol{x}_1) & \cdots & k(\boldsymbol{x}_1, \boldsymbol{x}_T) \\ & \vdots & \\ k(\boldsymbol{x}_T, \boldsymbol{x}_1) & \cdots & k(\boldsymbol{x}_T, \boldsymbol{x}_T) \end{bmatrix} \right) \tag{7}$$

GPs are completely characterized by a mean function $m(\boldsymbol{x}) \triangleq E[f(\boldsymbol{x})]$ and a covariance function

$$k(\boldsymbol{x}, \boldsymbol{x}') \triangleq E[(f(\boldsymbol{x}) - m(\boldsymbol{x}))(f(\boldsymbol{x}') - m(\boldsymbol{x}'))]$$

The posterior predictive distribution at the test data points for a GP prior as specified by Eq. (7) is also a Gaussian distribution [26]. In particular,

$$\boldsymbol{y}^{\text{tst}} | \boldsymbol{y}^{\text{trn}}, \boldsymbol{x}^{\text{trn}}, \boldsymbol{x}^{\text{tst}} \sim \mathcal{N}(\mu^{\text{tst}}, \Sigma^{\text{tst}}) \tag{8}$$

where

$$\mu^{\text{tst}} = K(\boldsymbol{x}^{\text{tst}}, \boldsymbol{x}^{\text{trn}})[K(\boldsymbol{x}^{\text{trn}}, \boldsymbol{x}^{\text{trn}}) + \sigma^2 I]^{-1} \boldsymbol{y}^{\text{trn}} \tag{9}$$

$$\Sigma^{\text{tst}} = K(\boldsymbol{x}^{\text{tst}}, \boldsymbol{x}^{\text{tst}}) - K(\boldsymbol{x}^{\text{tst}}, \boldsymbol{x}^{\text{trn}})[K(\boldsymbol{x}^{\text{trn}}, \boldsymbol{x}^{\text{trn}}) + \sigma^2 I]^{-1} K(\boldsymbol{x}^{\text{trn}}, \boldsymbol{x}^{\text{tst}}) \tag{10}$$

Here, $\boldsymbol{x}^{\text{trn}}$ and $\boldsymbol{y}^{\text{trn}}$ correspond to the training data for input and output variables, respectively, and $\boldsymbol{x}^{\text{tst}}$ and $\boldsymbol{y}^{\text{tst}}$ denote the input and output variables for the test data. The noise in the observation outputs is assumed to be additive, and it is modeled using independent and identically distributed Gaussian distributions with zero mean and variance σ^2. One of the most critical elements in formulating a GP model is the choice of an appropriate covariance kernel function, which models the correlation between any two points in the input space. An automatic relevance determination (ARD) formulation of the Matérn covariance function has been used in this work. The ARD formulation facilitates learning a length scale for each input dimension to deal with directional anisotropies in the dataset, and it has a shape parameter that can be tuned in order to control the smoothness of the correlation function in the input space. A shape parameter of $5/2$ has been used, which leads to the mathematical form

$$k(\boldsymbol{x}, \boldsymbol{x}'; \boldsymbol{\theta}) = \sigma_f^2 \left(1 + \sqrt{5}r + \frac{5}{3}r^2\right) \exp(-\sqrt{5}r)$$

where

$$r = \sqrt{\sum_{m=1}^{D} \frac{(x_k - x_k')^2}{\sigma_m^2}}$$

The hyperparameters in the kernel are $\boldsymbol{\theta} = [\sigma_f^2, (\sigma_m)_{k=1}^D]$, where D is the dimensionality of the data set; and σ_f and σ_m are the scaling coefficient and the characteristic length-scales, respectively.

Bayesian optimization is a surrogate modeling-based approach in which the black-box objective function is queried sequentially via *active learning*, and the posterior prediction of the GPs are updated with every new observation. Acquisition functions identify the new candidate points by striking a balance between exploration and exploitation. A high exploitation value suggests potentially high objective function values (for a maximization problem), whereas high exploration potential is exhibited by unexplored regions with high uncertainty. Expected improvement (EI) has been used to evaluate acquisition function values.

According to the formulation of Mockus [29] and Jones et al. [30], the EI acquisition function can be written as

$$\begin{aligned}EI(\boldsymbol{x}) &= (\mu(\boldsymbol{x}) - f(\boldsymbol{x}+) - \zeta)\phi(Z) + \sigma(\boldsymbol{x})\Phi(Z),\\ &\quad \text{if } \sigma(\boldsymbol{x}) > 0 \quad \text{and} \quad EI(\boldsymbol{x}) = 0, \ \text{if } \sigma = 0\end{aligned} \tag{11}$$

where

$$\begin{aligned}Z &= ((\mu(\boldsymbol{x}) - f(\boldsymbol{x}^+) - \zeta))/\sigma(\boldsymbol{x}),\\ &\quad \text{if } \sigma(\boldsymbol{x}) > 0 \text{ and } Z = 0 \text{ if } \sigma = 0\end{aligned} \tag{12}$$

where

$$\boldsymbol{x}^+ = \text{argmax}_{\boldsymbol{x}_i \in \boldsymbol{x}_{1:t}} f(\boldsymbol{x}_i)$$

is the input corresponding to the maximum functional value sampled until iteration t. Also, $\zeta > 0$ controls the tradeoff between global search and local optimization. Note that $\mu(x)$ and $\sigma(x)$ are the mean and variance, respectively, predicted by the GP for the input point $\boldsymbol{x}$. Also, ϕ and Φ are the probability density function and cumulative

distribution function of the standard normal distribution, respectively. A demonstration of this process has been provided in Fig. 3, where the following equation has been fitted by the GP:

$$y(x) = x\sin(7\pi x) \tag{13}$$

The blue line is the original function, and the red line is the posterior predictive mean of the GP. At each step, the optimization algorithm samples a new point based on the peak of the EI until convergence is reached in 15 steps (position of the optimum is shown with a red cross in Fig. 3). Confidence intervals are depicted by the yellow regions. It is noted that the uncertainty is lowest where a sample point exists. The confidence intervals become tighter as more points are sampled in the sequence (Fig. 3). The new point is sampled where the acquisition function hits a peak at

$$\boldsymbol{x}^{+} = \text{argmax}_{\boldsymbol{x}_i \in \boldsymbol{x}_{1:t}} f(\boldsymbol{x}_i)$$

C. Application of Bayesian Optimization Framework

Taking the square-shaped pin fin as the baseline (Fig. 1), each shape parameter (a, b, and c) was varied from 3.2 to 6 mm from the center of the square. A Python script was used to automate the workflow using ANSYS workbench (Fig. 4). For each design point, parametric changes in the design would translate to changes in the geometry, and subsequently the mesh. This would be followed by simulation in Fluent and return of the Nusselt number and friction factors for calculating the array efficiency.

An initial design of experiments (DOE) is selected using Latin hypercube sampling (LHS). A Reynolds-averaged Navier–Stokes (RANS) simulation is carried out for each of those design points. The surrogate model is initially trained with respect to this initial population. New design points are selected according to the acquisition function output after this initial training. Objective function values at these points are evaluated by performing a RANS simulation and a new surrogate model is obtained, which is improved by the Bayesian update. Three-row and four-row models of the pin-fin array were studied in the current problem, as rows 3–4 comprise the developing region of pin-fin arrays; and the highest heat transfer coefficients are observed in row 3 [4]. Since the optimization is carried out with a baseline case consisting of square-cross-section pin fins, the thermal performance efficiency is normalized with respect to $(Nu_1/f_1^{1/3})$, where Nu_1 and f_1 are the Nusselt number and friction factor values of the square ribbed geometries. The normalized objective function is henceforth represented as η':

$$\eta' = (Nu/Nu_1)/(f/f_1)^{1/3} \tag{14}$$

III. Results and Discussions

Figure 5 displays the input for the design of experiment points, which are used to train the GP surrogate model (blue dots) along with the optimal selection in the Bayesian optimization (BO) routine (red dots). A search space of 6000 points in three dimensions has been employed. Fifty-four initial points and five optimization points have been chosen in the routine according to a predefined budget. For the three-row model, 108 h of computation time was allotted to the initial DOE of 54 points. Each data point approximately consumed 2 h of wall time. Additionally, 10 h were assigned for the optimization routine. For the more computationally expensive four-row model, a cumulative 311 h of computation time was spent on the initial DOE of 64 points and 25 Bayesian optimization updates. The simulations were run on a computer with a six-core Intel core i-7 processor and 8 GB of RAM.

The initial points are selected by the LHS method based on an initially defined random seed, which ensures a decent spread in the search space for the initial DOE. The optimal points are sampled using the EI acquisition function at each stage of BO. The efficiency of each point is obtained from CFD simulations and passed into the GP model for training. Once the initial learning phase is over, the optimization iterations begin. Based on the predictions of the model in the global search space, the acquisition function selects the next point to sample based on a tradeoff between exploitation and exploration. Once an optimal point is selected, its efficiency is calculated using CFD and returned to the surrogate GP for retraining of parameters. Thus, the sequential process continues until a budget of five optimization steps is reached. As we can see from Fig. 5, the BO routine almost instantly picks up high-efficiency design points from the first optimization stage itself. A design point with the highest efficiency index of 1.472

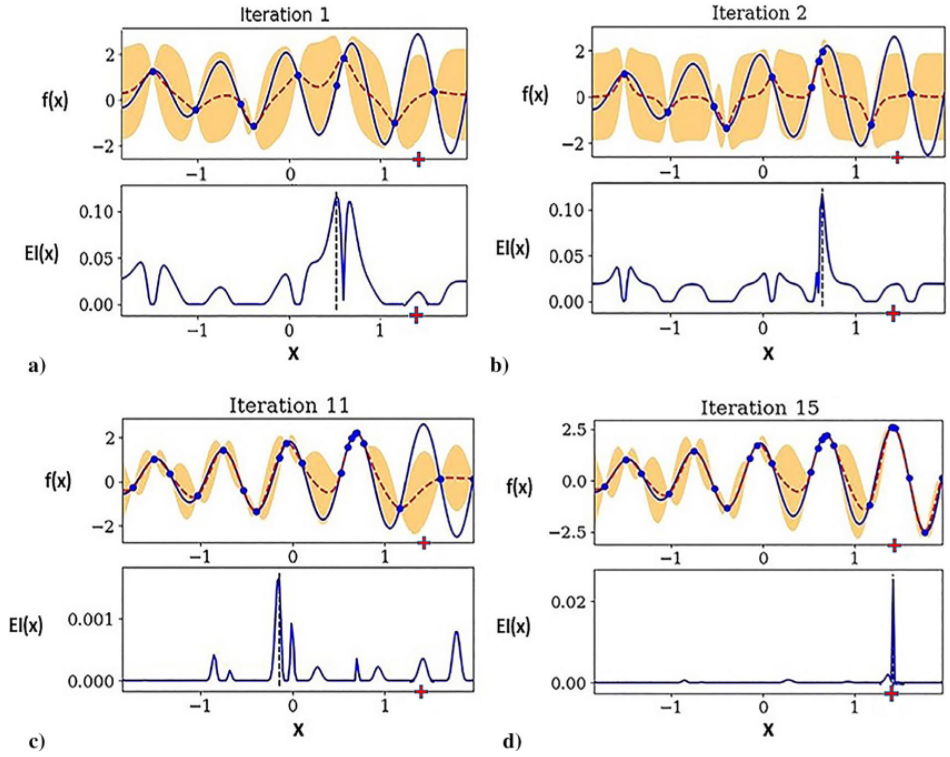

Fig. 3 Example of an iterative active learning problem: a) iteration 1, b) iteration 2, c) iteration 11, and d) iteration 15.

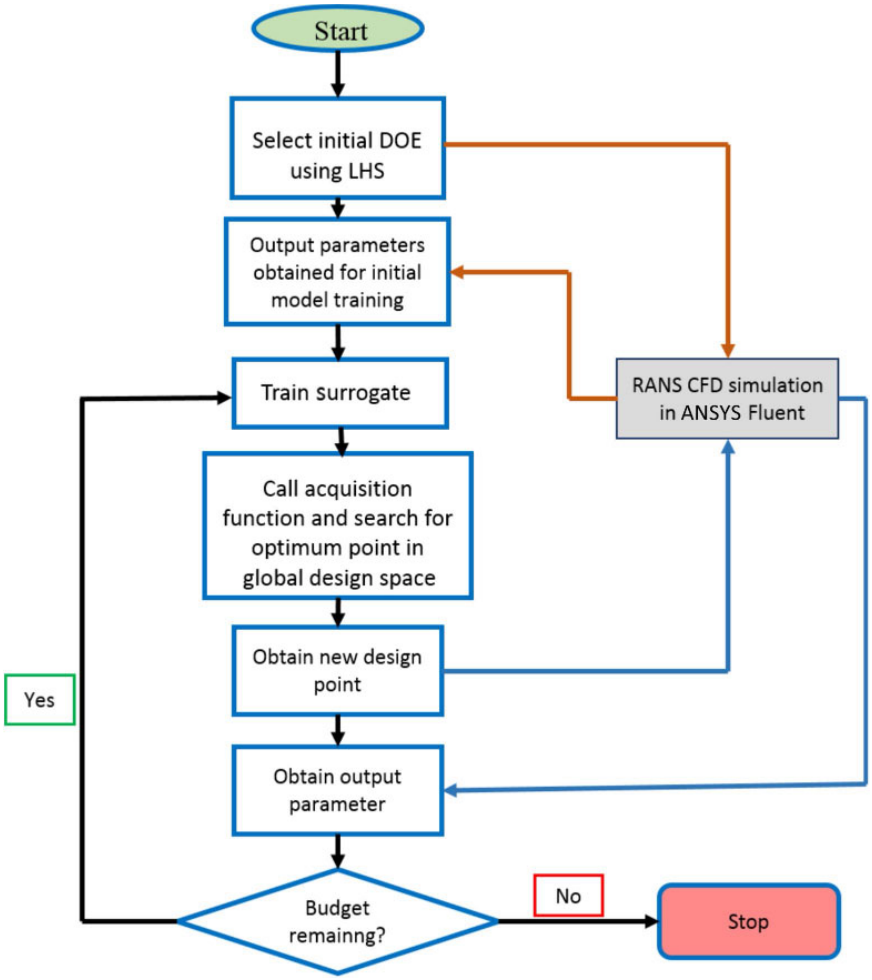

Fig. 4 Architecture of the proposed two-tier decision and control system.

that has $(a, b, c) = (5.983\ \text{mm}, 5.902\ \text{mm}, 3.382\ \text{mm})$ is picked up in the third optimization stage using this framework. A study was further performed to understand the effect of mesh size and the number of rows on the optimization results. Figure 6 lists the dimensions of the optimum pin fin, which were obtained with variations in the number of rows and mesh size in the baseline CFD model. Figure 5 shows the optimization results from the three-row model (case 2 from the table in Fig. 6). Similar types of shapes were obtained in all three cases with different base sizes and numbers of rows.

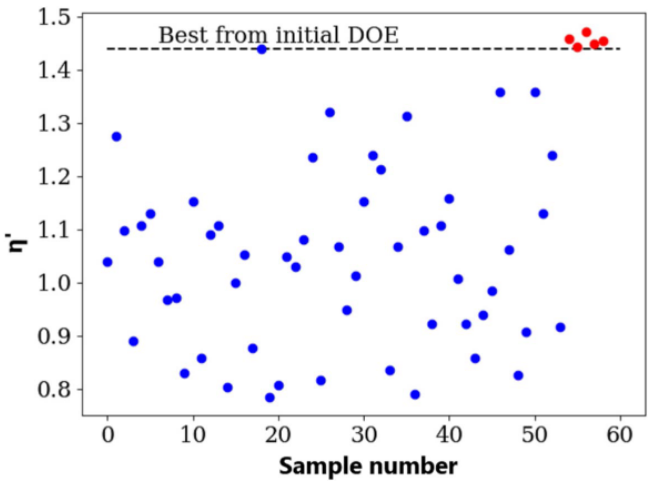

Fig. 5 Initial DOE points (blue dots), followed by the ones selected by Bayesian optimization (red dots). Dashed line shows baseline efficiency (maximum obtained from the initial DOE).

A. Comparison of Bayesian Optimization to Genetic-Algorithm-Based Optimization

The performance of the Bayesian optimization in finding optimal geometries has been compared with a multiobjective genetic algorithm (MOGA) optimizer inbuilt in ANSYS Workbench. The MOGA [31] is based on the nondominated sorted genetic algorithm–II (known as NSGA–II). Forty initial samples were generated, and the CFD solutions were calculated. Based on results of the objective function, 10 new samples were created in each iteration based on the fitness of each offspring. Five iterations were required to get a converged result. New offspring/populations are created by *selection*, *crossover*, or *mutation*. Each sample has a genetic representation, which is called a chromosome. This representation is usually an array of binary digits. The fitness function score is usually the objective function values possessed by each sample. Selection enables passing the current generation of samples to the next by selecting those with high fitness function values. Crossover combines two sets of parent chromosomes

Case	Base element size, mm	No. of rows in model	Optimum parameters, mm	Optimum shape
1	1.2	3	a=5.89, b=5.98, c=3.23	
2	0.9	3	a=5.89, b=5.90, c=3.38	
3	0.2	4	a=5.89, b=5.15, c=3.54	

Fig. 6 Variation of optimum shapes with change in mesh size/number of rows in array.

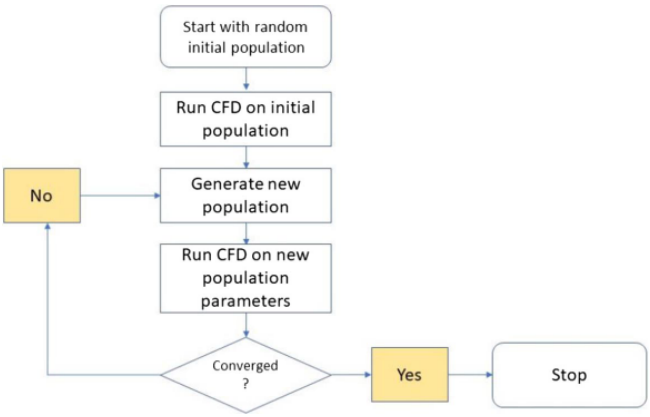

Fig. 7 Flowchart explaining schematics of MOGA.

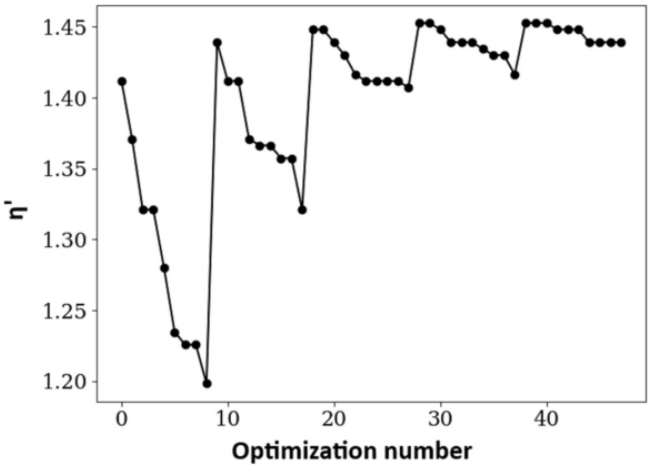

Fig. 8 Optimization cycle of MOGA: 50 sample points consist of five iterations with 10 samples in each iteration.

to produce a new offspring based on a user defined crossover probability, whereas mutation alters one or more gene values in a parent chromosome set, depending on the mutation probability. A crossover probability of 0.98 and a mutation probability of 0.01 were used. A high probability of crossover creates superior offspring but takes more time to converge. High mutation probabilities, on the other hand, create random populations. Figure 7 shows a flowchart explaining the operational principal of the MOGA.

Figure 5 shows the effectiveness of Bayesian optimization in finding optimal design locations with limited computational expense. It can be observed that within five iterations, it is possible to obtain a design corresponding to an efficiency of 1.472, whereas, it takes 30 iterations to reach a similar value (within 1.2%) of efficiency for the genetic-algorithm-based optimizer (Fig. 8). This showcases the computational advantage of the proposed optimization scheme under budget limitations, whereby optimal search locations can be possible to sample very early in the optimization stage. The MOGA optimization took 90 iterations (40 initial +50 optimization steps) to converge, whereas the Bayesian optimization took only 59 iterations to find an optimal design with efficiency 1.2% higher than that found by the MOGA. The surrogate model-based BO thereby saves computation time by 52%.

B. CFD Model and Mesh

The model of a four-row pin-fin array has been shown in Fig. 9. Sidewalls and the center planes have symmetry boundary conditions, whereas the endwall and pin surfaces have a constant-temperature no-slip condition. The CFD model used symmetry planes on two sidewalls as well as the middle plane of the geometry (Table 1). Symmetry planes help reduce the computational budget by reducing the domain size of the current problem. In the present scenario, it attempts to emulate an array that consists of multiple pin fins extending laterally to the sides. The symmetry boundary condition in the midplane further cuts down the wall-to-wall pin-fin domain into half. A velocity inlet was used with a fixed velocity of 12 m/s along with a zero-pressure outlet. A $k-\omega$ shear-stress transport turbulence model was employed to predict this highly turbulent flow, dominated by vortex structures from trailing-edge separation. Wall $y+$ values were less than three (Fig. 10). The CFD results were validated against experimental data from Chyu et al. [6] for the fully developed Nusselt number in the fourth row of the pin-fin array. The simulation underpredicted experimental data by 30%. This discrepancy can be attributed to both turbulence modeling errors and different downstream conditions for the experimental conditions as compared to the four-row CFD model. Ames and Dvorak [9] observed a RANS underprediction of the average Nusselt number by about 37% for the cylindrical pin-fin case at a similar Reynolds number when compared to the experimental case (which had an experimental uncertainty of 8%).

C. Comparison of CFD Results Between Optimal and Baseline Cases

Flow in pin-fin arrays is heavily dominated by vortex structures and local flow accelerations due to high amounts of blockage. A row averaged Nusselt number plot (Fig. 11) shows higher magnitudes in every location for the baseline case when compared to the optimum shape with higher-performance efficiency. The higher row-wise pressure-drop values (Fig. 12) of the baseline case can directly be attributed to the more aerodynamic shape of the optimum pin as compared to the bluff square baseline with its sharp edges. Since the efficiency parameter is a ratio between the Nusselt number and friction factor, the optimum case has a higher efficiency due to significant penalty of a higher-pressure drop in the baseline case.

Isometric Nusselt number contours are plotted to understand the local variations in heat transfer for the baseline and optimum shapes (Fig. 13). Isometric pressure contours of both the pin geometries show pressure peaks created at the stagnation points in the upstream sides of the pin fins due to impinging cooling air (Fig. 14). The same stagnation point can also be seen in the symmetry plane velocity contours (Fig. 15) and pressure contours (Fig. 16) along with low-pressure zones on the sidewalls of the pins. Midplane velocity contours

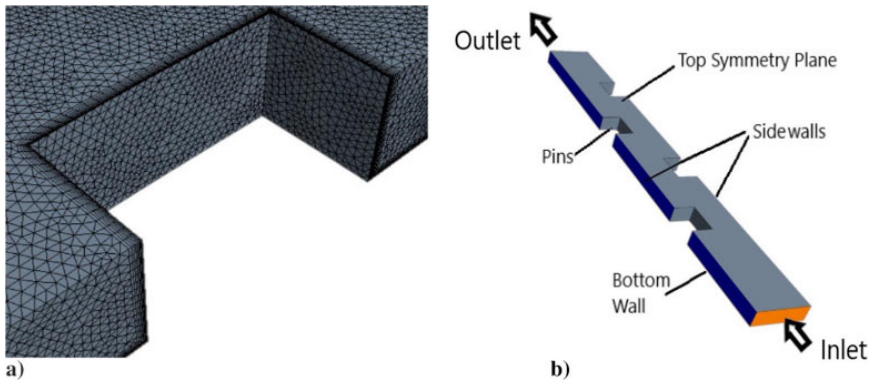

Fig. 9 Representations of a) zoomed-in view of mesh at pin with inflation layers and b) CFD domain with boundary conditions.

Table 1 CFD model details

Name of quantity/boundary	Description/number
Number of cells	1.1 million
Number of inflation layers	12
Base cell size	0.2 mm
Inlet condition	Constant velocity with 12 m/s; temperature = 300 K
Bottom wall	No-slip conditions; temperature = 350 K
Pins	No-slip conditions; temperature = 350 K
Side and top walls	Symmetry

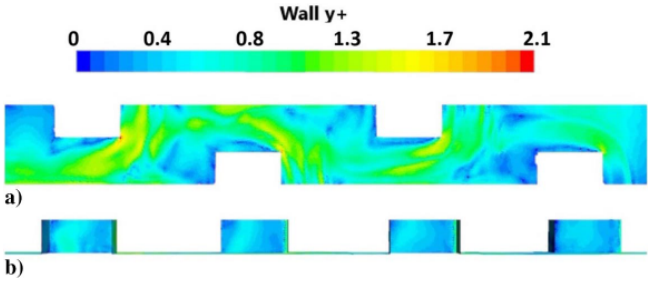

Fig. 10 Wall $y+$ values of baseline case.

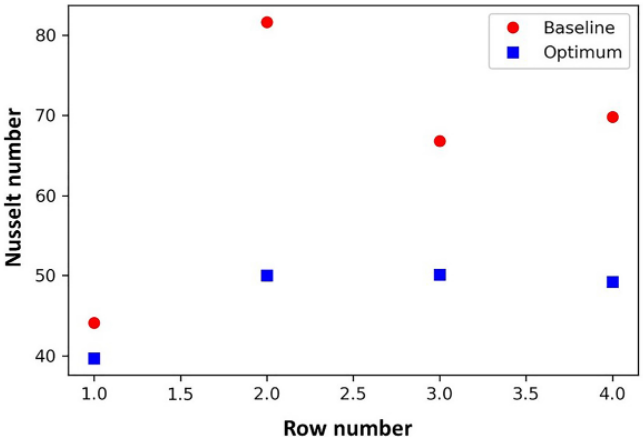

Fig. 11 Row-wise plot of Nusselt number for baseline and optimum cases.

(Fig. 15) show a separation zone forming at the same location as this pressure drop, which is represented in a deep-blue-colored low-velocity bubble. It should be noted that a larger separation bubble is visible in the baseline case due to flow detachment from the sharp corners of

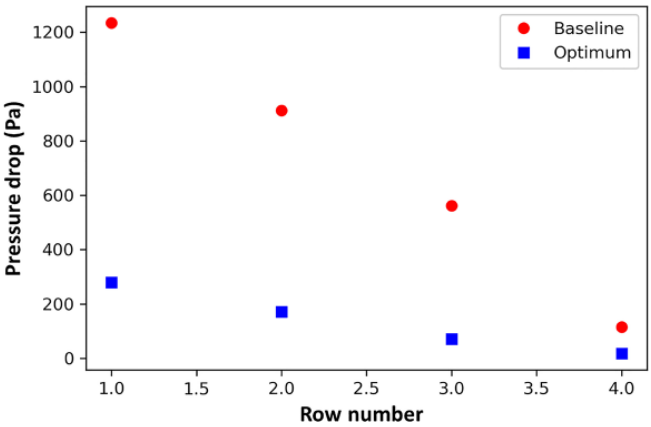

Fig. 12 Row-wise plot of pressure for baseline and optimum cases.

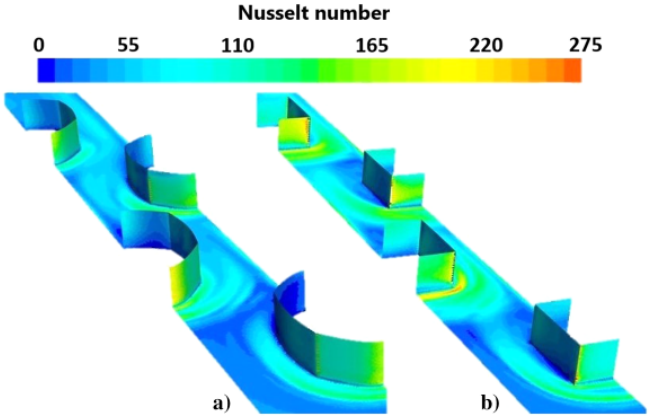

Fig. 13 Isometric plot of Nusselt number for a) optimized case and b) baseline case.

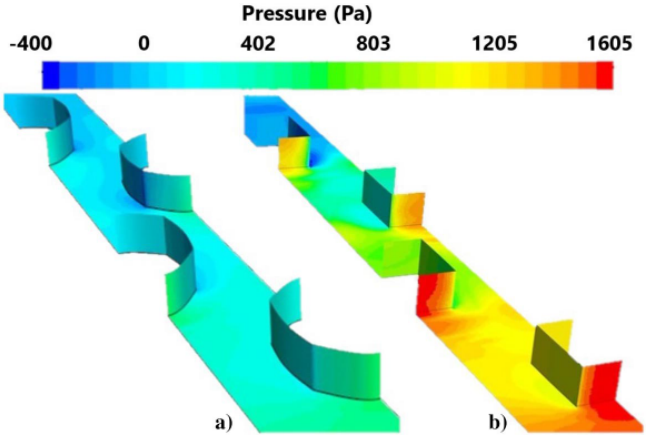

Fig. 14 Isometric plot of pressure for a) optimized case and b) baseline case.

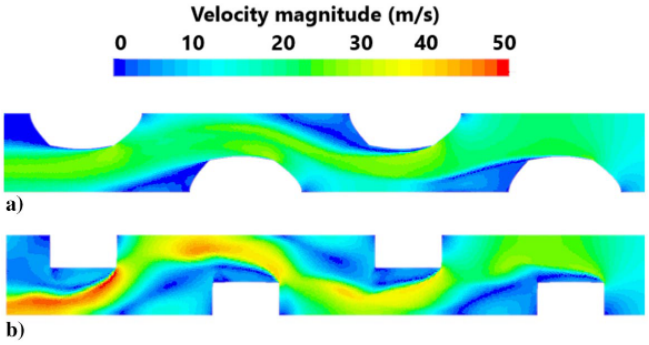

Fig. 15 Contour plot of a) midplane velocity optimized case and b) baseline case.

the square pins. Local acceleration is caused due to these flow separations, and they act as quasi blockages in addition to the flow obstacles created by the solid pin fins. Due to bigger separation zones in the baseline case, higher peaks of velocity can be seen compared to the optimum case (Fig. 15). Impingement of this locally accelerated flow in the downstream staggered pins is partially responsible for the higher heat transfer for the square baseline as seen in the isometric Nusselt number plots (Fig. 13).

To better understand the various flow phenomena behind heat transfer, row-wise heat transfer from pins and bottom walls were plotted separately for the two cases (Fig. 17). The change in pin-fin cross-section shapes was reflected more in the endwall heat transfer as compared to the heat loss from pins. In both cases, the endwall had a

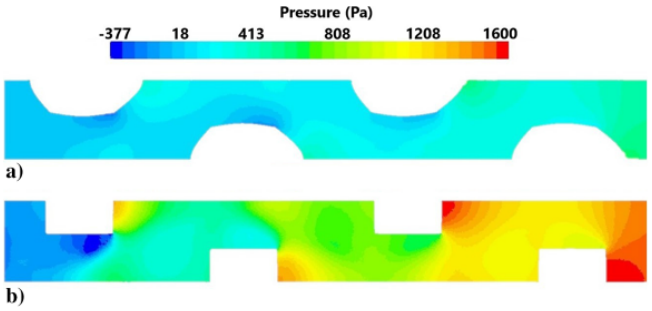

Fig. 16 Midplane pressure profile for baseline case of a) optimized case and b) baseline case.

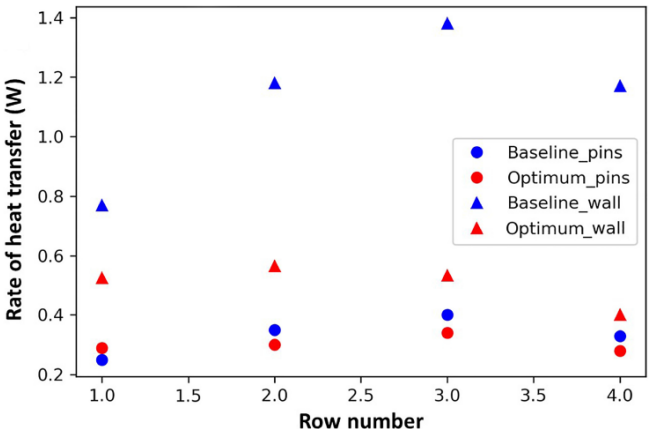

Fig. 17 Row-wise plot of heat transfer from pins and endwall.

higher heat transfer compared to the pin fins. Endwall Nusselt number plots (Fig. 18) showed peaks in the stagnation regions in the leading portions of the pins and in the regions with high blockage near the pin sidewalls, which coincides with the high-velocity flow regions (Fig. 19). Lower values are noticed beneath the separation bubble regions. However, the highest magnitude of the heat flux (Fig. 20) and Nusselt number is seen in the stagnation zones in horseshoe-like shapes. A near-wall plane of Q-criterion contours (Fig. 21) depicts the formation of coherent vortices for both the geometries. Jeong and Hussain [32] identified the Q criterion and Lambda-2 as the two most effective ways to identify coherent structures in turbulent flows. The vorticity magnitude is inadequate when it comes to identifying vortex cores, which contribute to the heat transfer augmentation in vortex-dominated turbulent flows. A threshold of the Q criterion and Lambda-2 criterion of the highest magnitude coherent structures were plotted to visually understand the horseshoe-type vortices at the leading edges. These vortices can be seen to extend beyond the pins, interact with the staggered pin downstream, and coincide with high heat transfer regions in Fig. 20 and high turbulent kinetic energy regions in Fig. 22. The threshold magnitudes were chosen to isolate the strong coherent structures from the other three-dimensional phenomena in this flow. Both the strength and size of these structures are greater in the square baseline case.

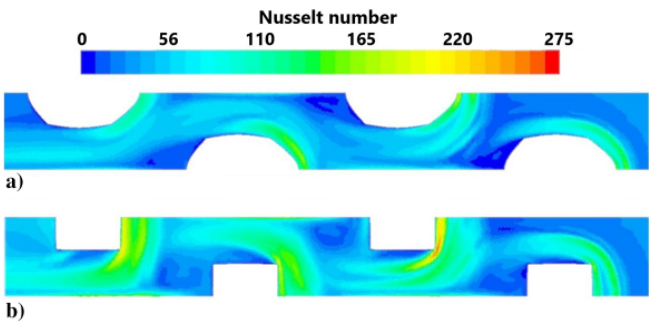

Fig. 18 Contour plot of endwall Nusselt numbers: a) optimized case and b) baseline case.

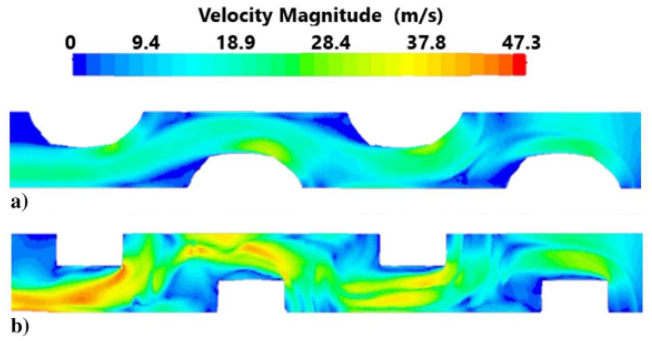

Fig. 19 Near-wall velocity magnitude for a) optimized case and b) baseline case.

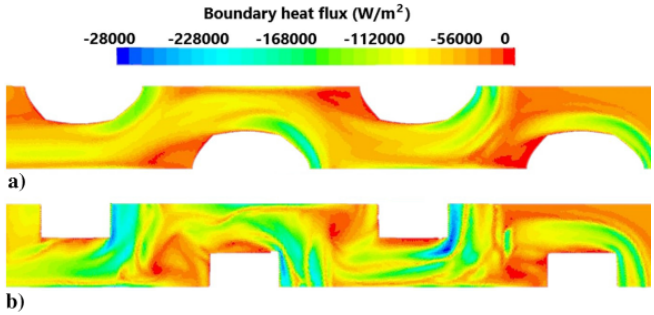

Fig. 20 Endwall heat flux: a) optimized case and b) baseline case.

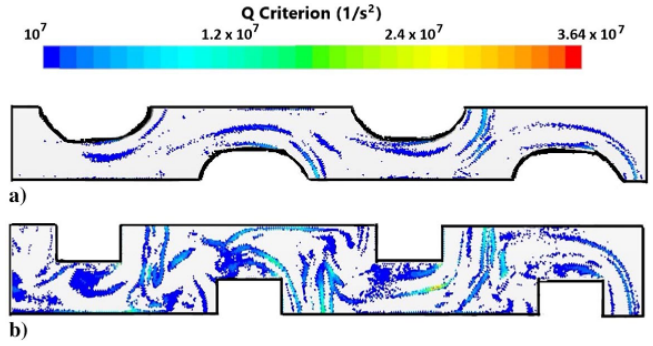

Fig. 21 Near-wall two-dimensional Q-criterion contours showing coherent vortex structures of a) optimized case and b) baseline case shown by isosurfaces of Lambda-2 criterion.

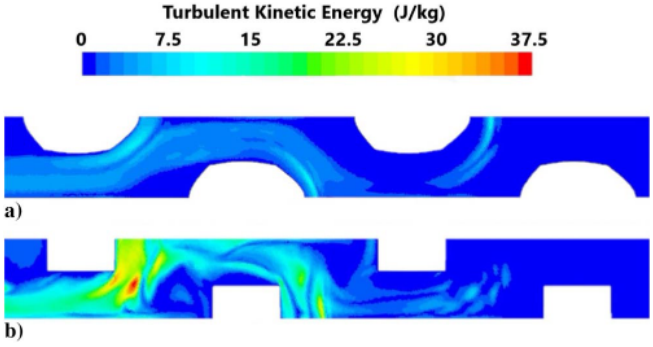

Fig. 22 Near-wall turbulent kinetic energy: a) optimized case and b) baseline case.

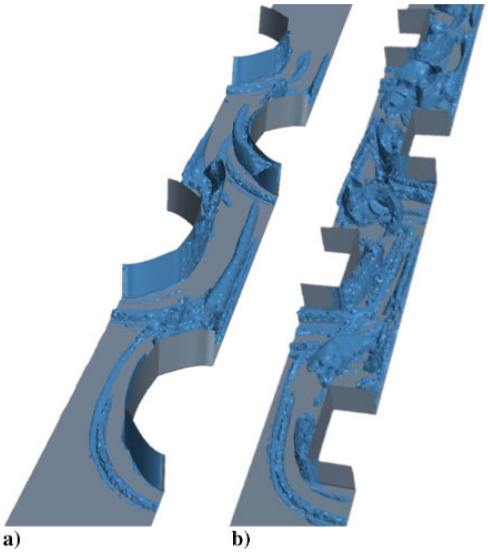

Fig. 23 Large vortical structures of a) optimized case and b) baseline case shown by isosurfaces of Lambda-2 criterion.

The Q criterion can be expressed as

$$Q = 1/2(|\Omega|^2 - |S|^2) \tag{15}$$

where Ω is the vorticity tensor, and S is the rate of strain tensor. Three-dimensional isosurfaces of the Lambda-2 criterion have also been used to obtain a global picture of coherent vortices as seen in Fig. 23. The Lambda-2 criterion is the second eigenvalue of the matrix comprising the sum of squares of the vorticity tensor and strain tensor; $\Omega^2 + S^2$. The higher presence of vortices results in higher turbulent mixing, as seen in the near-wall turbulent kinetic energy plots (Fig. 20) in the case of the square baseline pins. Hence, along with local flow accelerations due to blockages, such structures are also responsible for a higher loss of pressure in addition to increased heat transfer.

Most objective functions in real-world design problems have a black-box-type nature where a multidimensional design space needs to be explored in order to find a global optimum with a set of constraints. The current problem has a similar nature, except the constraint and the main objective variable have been lumped into one parameter based on existing literature [3]. The active learning approach that balances exploration vs exploitation to look for global optima can thus be a promising alternative to apply to practical optimization problems instead of existing gradient-based and gradient free optimization techniques. Besides predicting the optimum, BO can also create a surrogate model based on existing CFD results. Such a model has the potential to predict outputs at previously unknown design points with low computational time. This is another feature lacked by existing methods like the MOGA and is discussed further in the next section.

D. Training and Testing Performance of the Surrogate Model

A parity plot has been drawn to evaluate the accuracy of the surrogate model formed from the initial LHS and the Bayesian updates. It compares the value of the real simulation outputs with the predicted outputs. The four-row pin-fin array was used for training the surrogate model. Sixty-five initial points obtained from LHS were used to train the surrogate model initially, followed by 24 Bayesian updates. A high training R-squared score of 0.996 (Fig. 24a) suggests that the surrogate model has been properly trained, whereas a test R-squared score of 0.944 (Fig. 24b) shows that the model does not overfit and is capable of producing quite accurate predictions of the objective function. Overfitting occurs when the surrogate model is incapable of predicting data points outside of the training set, which results in a low test R-squared score. In the present study, R-squared scores of the training phase and the testing phase are within 5% of each other.

To further examine the effectiveness of the surrogate model, it was trained on the initial LHS space and an additional five Bayesian updates. The remaining 20 design points, which were the last 20 Bayesian updates in the optimization process, were used as input to this trained surrogate to examine the accuracy of prediction. The second parity plot shows the predicted vs actual values of the objective function for the last 20 Bayesian updates. A high R-squared score of 0.944 (Fig. 24b) suggests that the attempt to replace the CFD model with a surrogate trained from initial LHS and Bayesian optimization is promising. The surrogate model only takes a small fraction of the time compared to that of an actual CFD simulation. This has the potential to facilitate a method of efficient and time-saving prediction.

The novel surrogate model-based active learning approach demonstrated in the current work can be further improved by introducing a multifidelity approach that combines the results of high- and low-fidelity CFD models. Figure 25 shows the pressure drop vs Nusselt number plot for all the Bayesian update points. This plot demonstrates that a higher Nusselt number results in a higher-pressure drop too, and hence a constraint problem exists. A new approach modeling the pressure drop and Nusselt number using two different surrogate models will add more flexibility to the approach compared to the lumped approach in the current study. Another area of future work can be the inclusion of perforations in the pin fins. Maji et al. [33] concluded that porous pins of different shapes and pore shapes have a better heat transfer rate and a lower-pressure drop as compared to solid pins of similar shapes. The variation of pore shapes along with pin-fin shapes can lead to a more efficient pin-fin shape compared to the one obtained in this paper.

IV. Conclusions

A shape optimization has been carried out in the current study using surrogate modeling-based Bayesian optimization to improve

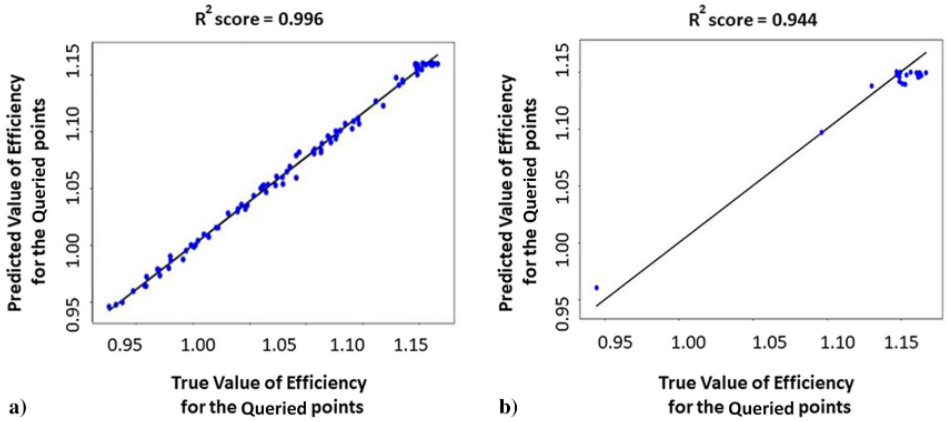

Fig. 24 Parity plots for the four-row CFD model: a) testing and b) training datasets.

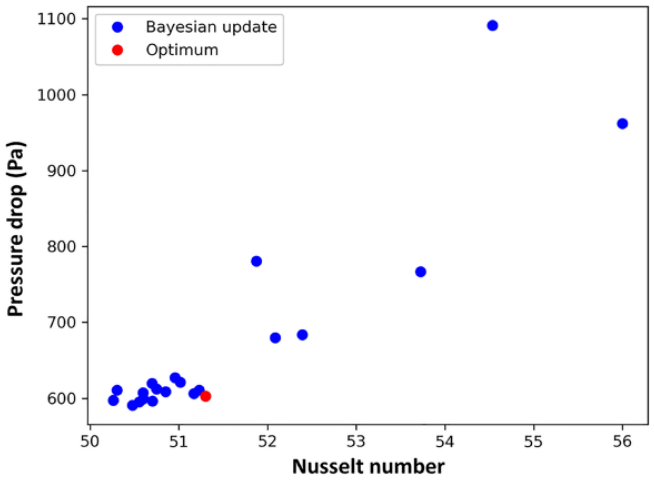

Fig. 25 Pressure drop vs Nusselt number (based on hydraulic diameter of channel) for the Bayesian updates.

thermal performance of a pin-fin array. A square-pin-fin rib geometry was considered as a baseline case to model the developing region of such an array. A three-dimensional design space has been explored by varying geometric parameters of each pin cross section. After training a Gaussian-process-based regression on the initial samples generated from Latin hypercube sampling, an exploration vs exploitation approach has been considered to reach an optimum. The results were then compared to the multiobjective genetic algorithm in ANSYS Workbench. The optimum objective function from Bayesian optimization was found to be 1.2% higher with 52% cheaper computational time, thereby indicating the efficacy of surrogate-based optimization in finding optimal design locations under budget limitations. The optimum pin-fin shape was found to have a smaller separation region size, ensuring uniform heat transfer and lower-pressure loss. The flow phenomenon governing the heat transfer was investigated by studying vortex structures using isosurfaces of Lambda-2 criterion. The more aerodynamic optimum shape attains a favorable compromise between pressure loss and heat transfer, thereby resulting in a higher value of the lumped efficiency parameter, which is effectively a ratio between heat transfer and pressure loss.

Acknowledgments

The authors want to thank the Florida Makes (award no. 70NANB15H041) and Florida High Tech Corridor programs (award no. AWD00000135) for funding this research. Any opinions, findings, and conclusions in this paper are those of the authors and do not necessarily reflect the views of the sponsoring agencies.

References

[1] Ligrani, P., "Heat Transfer Augmentation Technologies for Internal Cooling of Turbine Components of Gas Turbine Engines," *International Journal of Rotating Machinery*, Vol. 2013, March 2013, pp. 1–32. https://doi.org/10.1155/2013/275653

[2] Bunker, R. S., "Evolution of Turbine Cooling," *ASME Turbo Expo 2017: Turbomachinery Technical Conference and Exposition*, Vol. 1, American Soc. of Mechanical Engineers, Fairfield, NJ, 2017, p. V001T51A001. https://doi.org/10.1115/GT2017-63205

[3] Webb, R. L., and Eckert, E. R. G., "Application of Rough Surfaces to Heat Exchanger Design," *International Journal of Heat and Mass Transfer*, Vol. 15, No. 9, 1972, pp. 1647–1658. https://doi.org/10.1016/0017-9310(72)90095-6

[4] Chyu, M. K., "Heat Transfer and Pressure Drop for Short Pin-Fin Arrays with Pin-Endwall Fillet," *Journal of Heat Transfer*, Vol. 112, No. 4, 1990, pp. 926–932. https://doi.org/10.1115/1.2910502

[5] VanFossen, G. J., "Heat-Transfer Coefficients for Staggered Arrays of Short Pin Fins," *Journal of Engineering for Power*, Vol. 104, No. 2, 1982, pp. 268–274. https://doi.org/10.1115/1.3227275

[6] Chyu, M. K., Yen, C. H., and Siw, S., "Comparison of Heat Transfer from Staggered Pin Fin Arrays with Circular, Cubic and Diamond Shaped Elements," *ASME Turbo Expo 2007: International Gas Turbine Conference and Exhibit*, Vol. 4, American Soc. of Mechanical Engineers, Fairfield, NJ, 2007, pp. 991–999. https://doi.org/10.1115/GT2007-28306

[7] Metzger, D. E., Berry, R. A., and Bronson, J. P., "Developing Heat Transfer in Rectangular Ducts with Staggered Arrays of Short Pin Fins," *Journal of Heat Transfer*, Vol. 104, No. 4, 1982, pp. 700–706. https://doi.org/10.1115/1.3245188

[8] Metzger, D. E., and Haley, S. W., "Heat Transfer Experiments and Flow Visualization for Arrays of Short Pin Fins," *ASME 1982 International Gas Turbine Conference and Exhibit*, Vol. 4, American Soc. of Mechanical Engineers, Fairfield, NJ, 1982, p. V004T09A007. https://doi.org/10.1115/82-GT-138

[9] Ames, F. E., and Dvorak, L. A., "Turbulent Transport in Pin Fin Arrays: Experimental Data and Predictions," *Journal of Turbomachinery*, Vol. 128, No. 1, 2005, pp. 71–81. https://doi.org/10.1115/1.2098792

[10] Armstrong, J., and Winstanley, D., "A Review of Staggered Array Pin Fin Heat Transfer for Turbine Cooling Applications," *Journal of Turbomachinery*, Vol. 110, No. 1, 1988, pp. 94–103. https://doi.org/10.1115/1.3262173

[11] Venkata Rao, R., Saroj, A., and Bhattacharyya, S., "Design Optimization of Heat Pipes Using Elitism-Based Self-Adaptive Multipopulation Jaya Algorithm," *Journal of Thermophysics and Heat Transfer*, Vol. 32, No. 3, 2018, pp. 702–712. https://doi.org/10.2514/1.T5348

[12] Copiello, D., and Fabbri, G., "Multi-Objective Genetic Optimization of the Heat Transfer from Longitudinal Wavy Fins," *International Journal of Heat and Mass Transfer*, Vol. 52, Nos. 5–6, 2009, pp. 1167–1176. https://doi.org/10.1016/j.ijheatmasstransfer.2008.09.012

[13] Hajabdollahi, F., Rafsanjani, H. H., Hajabdollahi, Z., and Hamidi, Y., "Multi-Objective Optimization of Pin Fin to Determine the Optimal Fin Geometry Using Genetic Algorithm," *Applied Mathematical Modelling*, Vol. 36, No. 1, 2012, pp. 244–254. https://doi.org/10.1016/j.apm.2011.05.048

[14] Azarkish, H., Sarvari, S., and Behzadmehr, A., "Optimum Design of a Longitudinal Fin Array with Convection and Radiation Heat Transfer Using a Genetic Algorithm," *International Journal of Thermal Sciences*, Vol. 49, No. 11, 2010, pp. 2222–2229. https://doi.org/10.1016/j.ijthermalsci.2010.06.023

[15] Jha, R. K., and Chakraborty, S., "Genetic Algorithm-Based Optimal Design of Plate Fins Following Minimum Entropy Generation Considerations," *Journal of Mechanical Engineering Science*, Vol. 219, No. 8, 2005, pp. 757–765. https://doi.org/10.1243/095440605X31544

[16] Reddy, S. R., Abdoli, A., Dulikravich, G. S., Pacheco, C. C., Vasquez, G., Jha, R., Colaco, M. J., and Orlande, H. R. B., "Multi-Objective Optimization of Micro Pin-Fin Arrays for Cooling of High Heat Flux Electronics with a Hot Spot," *Heat Transfer Engineering*, Vol. 38, No. 56901, 2015, Paper V003T10A011. https://doi.org/10.1115/IPACK2015-48242

[17] Hamadneh, N., Khan, W. A., Sathasivam, S., and Ong, H. C., "Design Optimization of Pin Fin Geometry Using Particle Swarm Optimization Algorithm," *PLOS ONE*, Vol. 8, No. 5, 2013, pp. 1–9. https://doi.org/10.1371/journal.pone.0066080

[18] Eyi, S., Hanquist, K. M., and Boyd, I. D., "Aerothermodynamic Design Optimization of Hypersonic Vehicles," *Journal of Thermophysics and Heat Transfer*, Vol. 33, No. 2, 2018, pp. 392–406. https://doi.org/10.2514/1.T5523

[19] Eyi, S., Hanquist, K. M., and Boyd, I. D., "Shape Optimization of Reentry Vehicles to Minimize Heat Loading," *Journal of Thermophysics and Heat Transfer*, Vol. 33, No. 3, 2019, pp. 785–796. https://doi.org/10.2514/1.T5705

[20] Sacks, J., Welch, W. J., Mitchell, T. J., and Wynn, H. P., "Design and Analysis of Computer Experiments," *Statistical Science*, Vol. 4, No. 4, 1989, pp. 409–423. https://doi.org/10.1214/ss/1177012413

[21] Hevesi, J. A., Flint, A. L., and Istok, J. D., "Precipitation Estimation in Mountainous Terrain Using Multivariate Geostatistics. Part II: Isohyetal Maps," *Journal of Applied Meteorology*, Vol. 31, No. 7, 1992, pp. 677–688. https://doi.org/10.1175/1520-0450(1992)031<0677:PEIMTU>2.0.CO;2

[22] Kuya, Y., Takeda, K., Zhang, X., and Forrester, A. I., "Multifidelity Surrogate Modeling of Experimental and Computational Aerodynamic Data Sets," *AIAA Journal*, Vol. 49, No. 2, 2011, pp. 289–298. https://doi.org/10.2514/1.J050384

[23] Forrester, A. I., Sóbester, A., and Keane, A. J., "Multi-Fidelity Optimization via Surrogate Modelling," *Proceedings of the Royal Society of*

London, Series A: Mathematical, Physical and Engineering Sciences, Vol. 463, No. 2088, 2007, pp. 3251–3269. https://doi.org/10.1098/rspa.2007.1900

[24] Shahriari, B., Swersky, K., Wang, Z., Adams, R. P., and de Freitas, N., "Taking the Human Out of the Loop: A Review of Bayesian Optimization," *Proceedings of the IEEE*, Vol. 104, No. 1, 2016, pp. 148–175. https://doi.org/10.1109/JPROC.2015.2494218

[25] Shan, S., "Metamodeling Strategies for High-Dimensional Simulation Based Design Problems," Ph.D. Thesis, Dept. Mechanical and Manufacturing Engineering, Univ. of Manitoba, Winnipeg, MB, Canada, 2010.

[26] Rasmussen, C., and Williams, C., *Gaussian Processes for Machine Learning (Adaptive Computation and Machine Learning)*, MIT Press, Cambridge, MA, 2005.

[27] Di Nicola, G., Pierantozzi, M., Petrucci, G., and Stryjek, R., "Equation for the Thermal Conductivity of Liquids and an Artificial Neural Network," *Journal of Thermophysics and Heat Transfer*, Vol. 30, No. 3, 2016, pp. 651–660. https://doi.org/10.2514/1.T4863

[28] Madoliat, R., Razavi, M., and Dehghani, A. R., "Modeling of Heat Transfer in Cisterns Using Artificial Neural Networks," *Journal of Thermophysics and Heat Transfer*, Vol. 23, No. 2, 2009, pp. 411–416. https://doi.org/10.2514/1.37043

[29] Mockus, J., "On Bayesian Methods for Seeking the Extremum," *Proceedings of the IFIP Technical Conference*, Vol. 27, *Lecture Notes in Computer Science*, Springer-Verlag, London, 1974, pp. 400–404. https://doi.org/10.1007/3-540-07165-2_55

[30] Jones, D. R., Schonlau, M., and Welch, W. J., "Efficient Global Optimization of Expensive Black-Box Functions," *Journal of Global Optimization*, Vol. 13, No. 4, 1998, pp. 455–492. https://doi.org/10.1023/A:1008306431147

[31] Deb, K., *Multi-Objective Optimization Using Evolutionary Algorithms*, Wiley, New York, 2001.

[32] Jeong, J., and Hussain, F., "On the Identification of a Vortex," *Journal of Fluid Mechanics*, Vol. 285, Feb. 1995, pp. 69–94. https://doi.org/10.1017/S0022112095000462

[33] Maji, A., Bhanja, D., Patowari, P. K., and Kundu, B., "Thermal Analysis for Heat Transfer Enhancement in Perforated Pin Fins of Various Shapes with Staggered Arrays," *Heat Transfer Engineering*, Vol. 40, Nos. 3–4, 2019, pp. 295–319. https://doi.org/10.1080/01457632.2018.1429047